J Mater Sci (2020) 55:17081–17093

Energy materials

Cation-adsorption-assisted Ni_3S_2/carbon nanowalls composites with three-dimensional interconnected porous structures for high-performance lithium-ion battery anodes

Hai-Jun Chen[1], Yan Wang[1,*], Xu-Dong Ma[2], Cong Fan[1,*], Pei Kang Shen[2], Shi-Wo Ta[3], Hai-Bin Wu[3], and Zhe-Sheng Feng[1,*]

[1] *School of Materials and Energy, University of Electronic Science and Technology of China, Chengdu 610054, People's Republic of China*
[2] *Collaborative Innovation Center of Sustainable Energy Materials, Guangxi University, Nanning 530004, People's Republic of China*
[3] *State Key Laboratory of Advanced Materials and Electronic Components, Guangdong Fenghua Advanced Technology Holding Company Limited, Zhaoqing 526000, People's Republic of China*

Received: 7 May 2020
Accepted: 30 August 2020
Published online:
22 September 2020

ABSTRACT

Metal sulfide/carbon composite reveals to be a prospective electrode material for lithium-ion batteries due to the synergy of the two components, and their structure greatly determines the electrochemical performance. We herein have successfully fabricated an in situ encapsulation of Ni_3S_2 nanoparticles into carbon nanowalls (Ni_3S_2/CNWs) with three-dimensional interconnected porous structures, which are synthesized assisted by cation adsorption and following hydrothermal process. The abundant mesoporous carbon nanowalls are used as both conductive matrix and protective layer to alleviate the volume change of Ni_3S_2. Benefiting from the superior theoretical capacity of Ni_3S_2 and unique structure of CNWs, Ni_3S_2/CNWs-1 anodes show the high discharge capacity of 906 mAh g^{-1} at 200 mA g^{-1} after cycling 200 times, outstanding rate capacity of 567 mAh g^{-1} at 5 A g^{-1} and super-long cycling life of 666 mAh g^{-1} at 2 A g^{-1} after cycling 1000 times. More importantly, the button-type full cells based on Ni_3S_2/CNWs-1 anodes and $LiFePO_4$ cathodes present excellent cycling stability and practicality.

Handling Editor: Mark Bissett.

Address correspondence to E-mail: wy@uestc.edu.cn; fancong@uestc.edu.cn; fzs@uestc.edu.cn

https://doi.org/10.1007/s10853-020-05203-3

Introduction

Lithium-ion batteries (LIBs) have been proved to be the main power source for portable electronic devices and hybrid electric vehicles due to their advantages of high energy density, long cycling life and environmental benignity [1–3]. Nevertheless, the theoretical capacity of commercialized graphite anode is just as low as 372 mAh g^{-1}, which leads to the fact that the presently available LIBs are unable to further satisfy the requirements of large-scale energy storage [4, 5]. Consequently, considerable efforts have been devoted to develop the innovative anode materials for high-performance LIBs. Nowadays, transition metal sulfides, such as Ni_3S_2, NiS, NiS_2, CoS_2 and Co_9S_8 [6–9], have been regarded as possible candidates and attracted tremendous attention due to their multistep reversible redox reactions, which provide high theoretical capacity by making full use of all oxidation states of transition metals to achieve storage conversion reactions mechanism. Among them, Ni_3S_2 with the merits of superior theoretical capacity (446 mAh g^{-1}), abundant resources and low cost shows great potentiality as a favorable anode of LIBs [10, 11]. Nevertheless, both its inferior electronic conductivity and severe volume change during the cycling all lead to extremely poor rate performance and fast capacity fading. The common strategies for solving the above drawbacks include coating with carbon layer, designing various Ni_3S_2 nanostructures, anchoring onto a conductive substrate, constructing metal sulfide composites and so on [12, 13]. These strategies can enhance lithium storage capability of electrode materials. For instance, Li et al. had successfully fabricated a heterostructure of NiO nanosheet array grown on β-NiS@Ni_3S_2 framework by a simple hydrothermal synthesis. The prepared NiO@β-NiS@Ni_3S_2 composite exhibits excellent lithium storage as the anode material of LIB [14]. Yang et al. reported a novel heterogeneous structure of NiO/Ni_3S_2 nanoflake composite with a carbon nanofiber (CNF) membrane. The binderless NiO/Ni_3S_2/carbon nanofiber electrode shows the excellent lithium storage capability [15]. Although the advancement in the LIB anodes of Ni_3S_2-based materials had been achieved, investigating the novel electrodes with superior capacity and cycle capability remains an immense challenge of high-performance LIBs.

In recent years, carbon nanowalls (CNWs) are an emerging material that is vertically aligned and assembled from carbon nanosheets. The preferable conductivity and three-dimensional (3D) porous structure of carbon nanowalls not provide the inherent advantages of two-dimensional carbon nanosheet, prevent the agglomeration of nanoparticles, but enhance the permeability of electrolyte and thus shorten the distance of Li-ion diffusion, especially in an abundant mesoporous structure [16, 17]. Consequently, in situ combining transition metal sulfide and carbon nanowalls to prepare the composite structure were confirmed to be an efficacious approach to optimize the rate capability and cycle stability of electrodes.

We, herein, have elaborated an in situ encapsulation of Ni_3S_2 nanoparticles into carbon nanowalls with 3D porous structures through a cation-adsorption approach and a hydrothermal synthesis. In this synthesis process, cation exchange resin as a carbon source can sufficiently absorb nickel ions. The catalytic nickel ions are used to catalyze the growth of carbon nanowalls during the heat treatment process. Equally important, the alkaline $KHCO_3$ acts as a pore-forming agent not only determines the contents of Ni_3S_2 and CNWs, but also enables the cation exchange resin to form large surface area and abundant mesoporous structure. Therefore, the adsorbed nickel ions and the pore-forming agent of $KHCO_3$ both play important roles in the formation of Ni_3S_2/CNWs. The 3D-interconnected porous carbon nanowalls, as an electrically conductive and buffered matrix, enhance the electrochemical activity and structural stability of the Ni_3S_2, and effectually prevent the pulverization and aggregation of Ni_3S_2 nanoparticles. The Ni_3S_2/CNWs-1 composite shows remarkable electrochemical performance, which is ascribed to the synergistic combination of well distributed Ni_3S_2 nanoparticles and conductive carbon nanowalls. In this contribution, our ingenious approach not only highlights an effective strategy to stabilize metal sulfides but also paves the way for the further improvement of lithium-ion battery composite electrode materials.

Experimental section

Synthesis of Ni/CNWs precursor and CNWs

All related reagents were used without further purification and purchased from Macklin. The Ni/

CNWs precursor was synthesized by a cation adsorption approach. Typically, 0.04 mol of nickel acetate is dissolved in 400 mL of deionized water, followed by the addition of 20 g of cation exchange resin and magnetic stirring for 8 h. Thereafter, the resin was dried at 80 °C overnight. The dried product was pulverized into powder by a pulverizer, then transferred to a solution with 60 g $KHCO_3$ in 300 mL ethanol and heated to 90 °C to remove moisture. The obtained product was heated to 850 °C in a nitrogen atmosphere and kept for 1 h. After complete cooling, the Ni/CNWs precursor was cleaned to neutral repeatedly with ethanol and deionized water and then dried overnight in a vacuum drying oven. In addition, the CNWs sample was obtained by adding Ni/CNWs precursor in 3 M hydrochloric acid solution and stirring strongly for 10 h to completely remove impurities and nickel elements.

Preparation of Ni_3S_2/CNWs and Ni_3S_2

Ni_3S_2/CNWs was done by a hydrothermal process. In general, 0.25 g of Ni/CNWs precursor and 16 mmol of thiourea were added to 80 ml of deionized water. After stirring well, the solution was transferred to an autoclave followed by heating at 180 °C for 16 h. The cooled product was filtered several times with ethanol and deionized water and then dried in a vacuum-drying oven overnight. Eventually, in order to increase the crystallinity, the sample was heated to 500 °C under a nitrogen atmosphere and kept for 2 h to obtain the Ni_3S_2/-carbon nanowalls (designated as Ni_3S_2/CNWs-1).

As a comparison, Ni_3S_2/CNWs-2 was prepared by the same synthesis method, except increasing the amount of $KHCO_3$ to 120 g. Additionally, Ni_3S_2 sample was prepared by the above method except that 24 mmol of nickel acetate was used instead of 0.25 g Ni/CNWs precursor.

Physical characterization

The crystal structures were studied by X-ray diffraction (XRD, Rigaku Corporation SmartLab Studio II) with a Cu Kα radiation. The morphologies and microstructures were determined using a scanning electron microscope (SEM, Hitachi SU8220) and a transmission electron microscope (TEM, FEI Titan ETEM G^2) with high-performance X-ray energy-dispersive spectrometer (EDS). Thermogravimetric (TGA, NETZSCH-Gerätebau GmbH Company) analysis was carried out from room temperature to 1000 °C in the air at a heating rate of 10 °C min^{-1} to determine the Ni_3S_2 content in Ni_3S_2/CNWs composite. Raman analyses were performed on a Raman spectrometer (Horiba Jobin Yvon Company) from 600 to 4000 cm^{-1} with a 532 nm laser. The elemental compositions and valence state were characterized by X-ray photoelectron spectroscopy (XPS, Thermo Fisher Scientific Corporation Escalab 250Xi) with a monochromatic Al Kα radiation. The ASAP-2460 surface area analyzer (Micromeritics Instrument Corporation) uses Brunauer–Emmett–Teller (BET) method to obtain specific surface area.

Electrochemical measurements

With the aim of testing the electrochemical properties of the samples, the CR2025 button-type half-cells were assembled in an argon-filled glove box (Mikrouna company). The active material, carbon black and poly(vinylidene fluoride) (PVDF) were mixed with N-methyl-2-pyrrolidinone (NMP) at a mass ratio of 8:1:1 to form a uniform slurry to prepare the working electrodes. The prepared slurry was coated on a Cu foil and dried at 70 °C overnight. The separator, current collector and counter electrode were Celgard 2400, copper foil and Li metal foil, respectively. The electrolyte was a mixture of 1 M $LiPF_6$ dissolved in ethylene carbonate (EC)/dimethyl carbonate (DMC) (v/v = 1:1). For button-type full cell assembly, the commercial $LiFePO_4$ cathode (GEELY Corp.) was used instead of the metallic lithium. The $LiFePO_4$ cathode was prepared under the same procedure as the preparation of Ni_3S_2/CNWs-1 anode. For the purpose of matching the capacity of cathode and anode electrodes, the capacity of anode electrodes is slightly excessive compared with that of cathode electrodes, and the capacity of Ni_3S_2/CNWs-1 anode to $LiFePO_4$ cathode was about 1.2:1. Before the preparation of the full cell, the pre-lithiation of Ni_3S_2/CNWs-1 anodes was carried out in five charge and discharge cycles. A Neware battery testing system performs charge and discharge measurements. Cyclic voltammetry (CV) curves were obtained in the potential range of 0.01–3.00 V at 0.1 mV s^{-1} and electrochemical impedance spectroscopy (EIS) was conducted in the frequency range of 10^5–0.01 Hz using a Zennium IM6 electrochemical workstation.

Results and discussion

The whole preparation route of Ni_3S_2/CNWs composite is shown in Fig. 1, which includes four steps: (1) Ni^{2+} cations were completely adsorbed to the pretreated cation exchange resin; (2) the dried resin was pulverized and then immersed in the $KHCO_3$/ethanol mixture; (3) in the calcination process, Ni/CNWs precursor was fabricated by $KHCO_3$ pore-forming agent; (4) the Ni nanoparticles were sulfurized into uniform Ni_3S_2 by a controlled hydrothermal reaction and then annealed to increase the crystallinity of Ni_3S_2/CNWs.

The XRD pattern of Ni_3S_2/CNWs-1 sample is displayed in Fig. 2a. The peaks at 21.8°, 31.2°, 37.9°, 44.5°, 49.9°,55.3°, 64.5°, 69.2°, 73.3° and 78.1° can be well indexed to the (100), (1–10), (111), (200), (210), (2–11), (220), (300), (310) and (1–31) planes of the rhombohedral Ni_3S_2 structure [18], and a weak peak at 26.2° is ascribed to the (002) plane of the hexagonal graphite structure, which are consistent with the XRD standard data cards of JCPDS No.73-0698 and JCPDS No.75-1621, respectively. The sharp and intense peaks signify highly crystalline of as-synthesized samples. In addition, Fig. S1 displays that all diffraction peaks of the Ni/CNWs precursor can be accurately indexed to the cubic Ni crystal of JCPDS No.87–0712, indicating that the precursor can be successfully converted to Ni_3S_2 by the vulcanization process. All diffraction peaks of the control sample Ni_3S_2 (Fig. S2) were identical to Ni_3S_2 in Ni_3S_2/CNWs samples.

The morphology and microstructure of Ni_3S_2/CNWs-1 composites were investigated by FE-SEM. The Ni_3S_2 nanoparticles (Fig. 2b, c) are uniformly embedded in highly conductive porous carbon nanowalls. It is further observed from the low-resolution TEM image (Fig. 2d) that the Ni_3S_2 nanoparticles are uniformly dispersed in 3D-interconnected carbon nanowalls, which can significantly strengthen the electrical conductivity and structural stability of Ni_3S_2/CNWs-1. In the Ni_3S_2/CNWs-1 composite, the carbon nanowall is composed of 6 layers of 1.7-nm-thick carbon layer, as displayed in the higher-resolution TEM in Fig. 2e, f. The (200) crystal plane of the Ni_3S_2 phase and (002) face of the graphitic carbon (Fig. 2f) is corresponding to the interplanar spacing of 0.20 and 0.34 nm, respectively, which are in accordance with the XRD results. The polycrystalline nature of Ni_3S_2 is reflected by the corresponding fast Fourier transformation (FFT) diffraction pattern (the inset of Fig. 2f). Furthermore, the selected area electron diffraction (SAED) pattern (Fig. S3) of Ni_3S_2/CNWs-1 composite shows three diffraction rings, which can be assigned to the (1–10), (1–21) and (321) crystal planes of Ni_3S_2, respectively. The morphology of Ni/CNWs precursor (Fig. S4) is identical to that of Ni_3S_2/CNWs-1, which indicates that the original structure is preserved perfectly during the hydrothermal synthesis procedure. The morphology

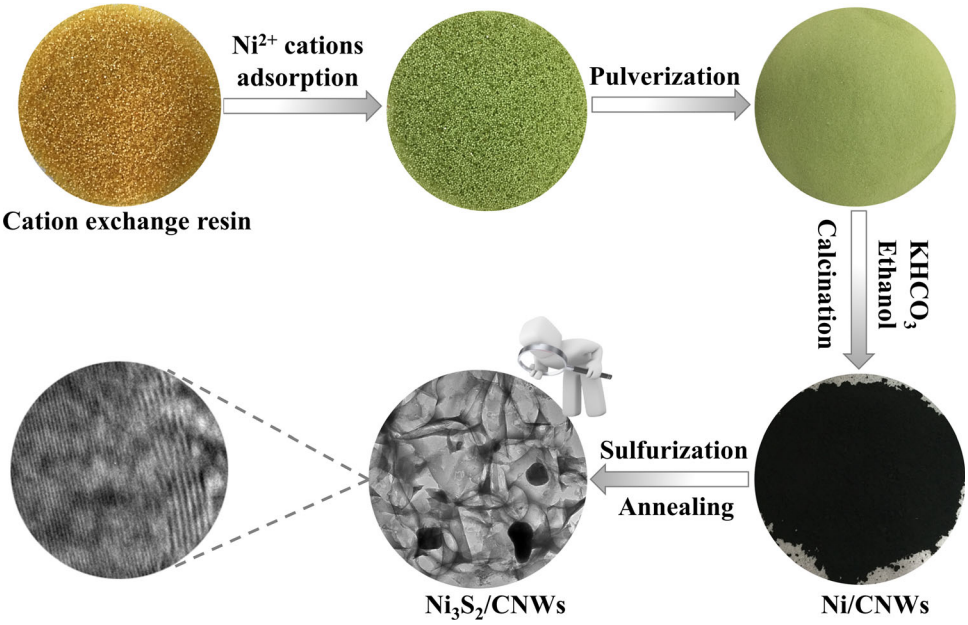

Figure 1 Schematic diagram of the fabrication of Ni_3S_2/CNWs composites.

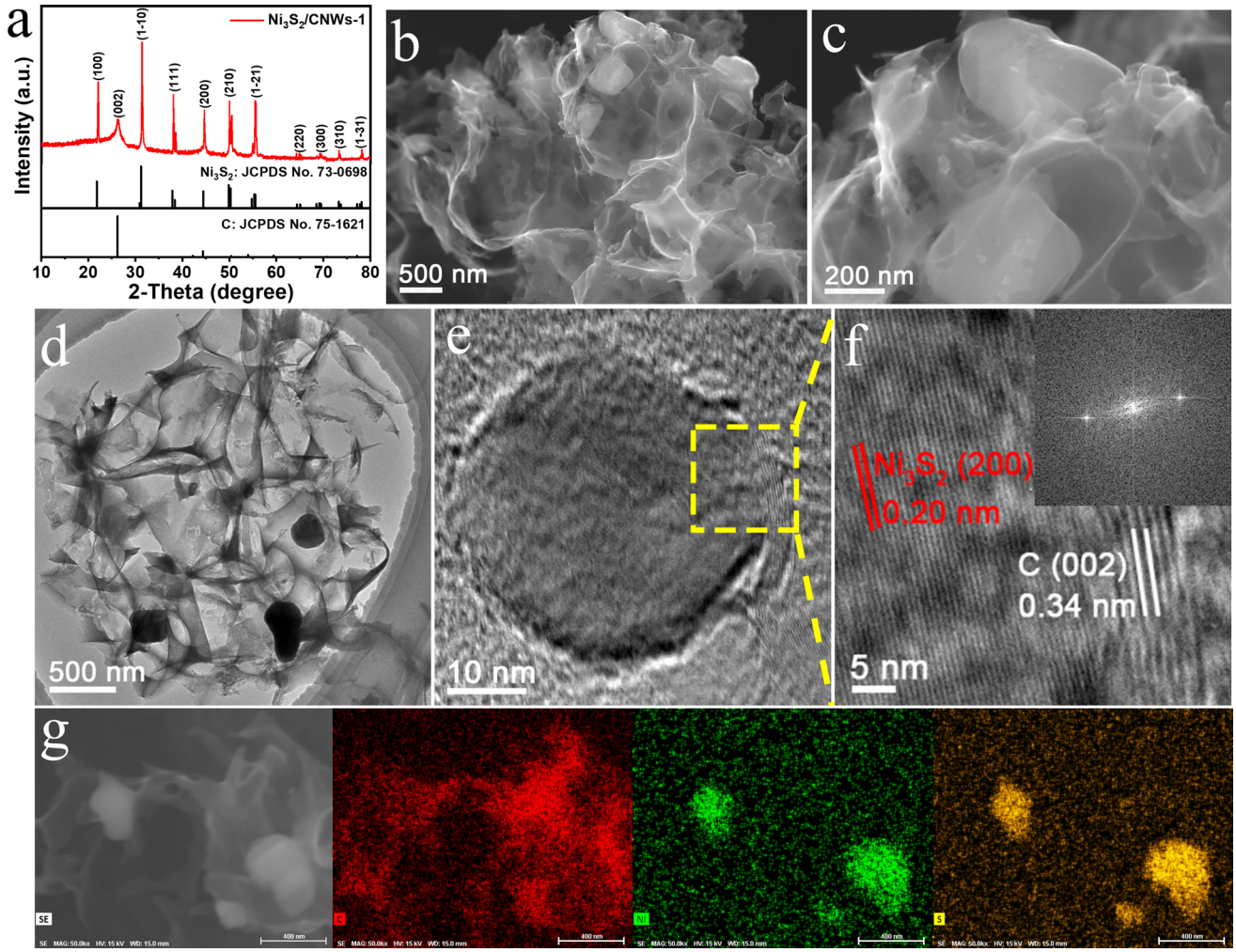

Figure 2 **a** XRD patterns; **b**, **c** SEM images; **d** low-resolution TEM images and **e**, **f** HRTEM images of Ni_3S_2/CNWs-1 composite (the inset showing the corresponding FFT pattern of Ni_3S_2); **g** elemental mapping results of Ni_3S_2/CNWs-1.

of Ni_3S_2/CNWs-2 (Fig. S5) is almost homologous to the Ni_3S_2/CNWs-1. The control sample Ni_3S_2 (Fig. S6) shows an irregular shape. From the SEM images (Fig. S7), it is observed that CNWs presents a crumpled and 3D-interconnected porous structure, which may be attributed to the production of carbon dioxide and water during the pyrolysis of pore-forming agent of $KHCO_3$. The EDS element mapping of the TEM image is displayed in Fig. 2g, from which we can observe that the C, Ni and S elements are homogeneously dispersed in the Ni_3S_2/CNWs-1 composite. Combined with XRD and HRTEM results, Ni_3S_2/CNWs-1 was prepared successfully. Additionally, element analysis of Ni_3S_2/CNWs-1 and Ni_3S_2/CNWs-2 composites was investigated via employing EDS spectroscopy, and the results are shown in Fig. S8. The atomic percentages of carbon, nickel and sulfur elements in Ni_3S_2/CNWs-1 are 88.64, 7.07 and 4.29 at%, respectively. The molar ratio of nickel to sulfur is about 3:2 and further confirms the formation of pure Ni_3S_2, which also coincides with XRD result. The contents of Ni_3S_2 and CNWs in the Ni_3S_2/CNWs-1 composite was determined by TGA analysis. As shown in Fig. 3a, the initial slight weight loss below 400 °C can be attributed to the evaporation of water and the removal of residual organics, and the subsequent weight loss from 400 to 650 °C corresponds to the consumption of CNWs and the conversion of Ni_3S_2 to NiO. According to the 26.9 wt% of the original mass percentage remained after TGA analysis, the contents of Ni_3S_2 and CNWs in the Ni_3S_2/CNWs-1 sample are calculated to be 28.8 and 71.2 wt%, respectively, and the corresponding

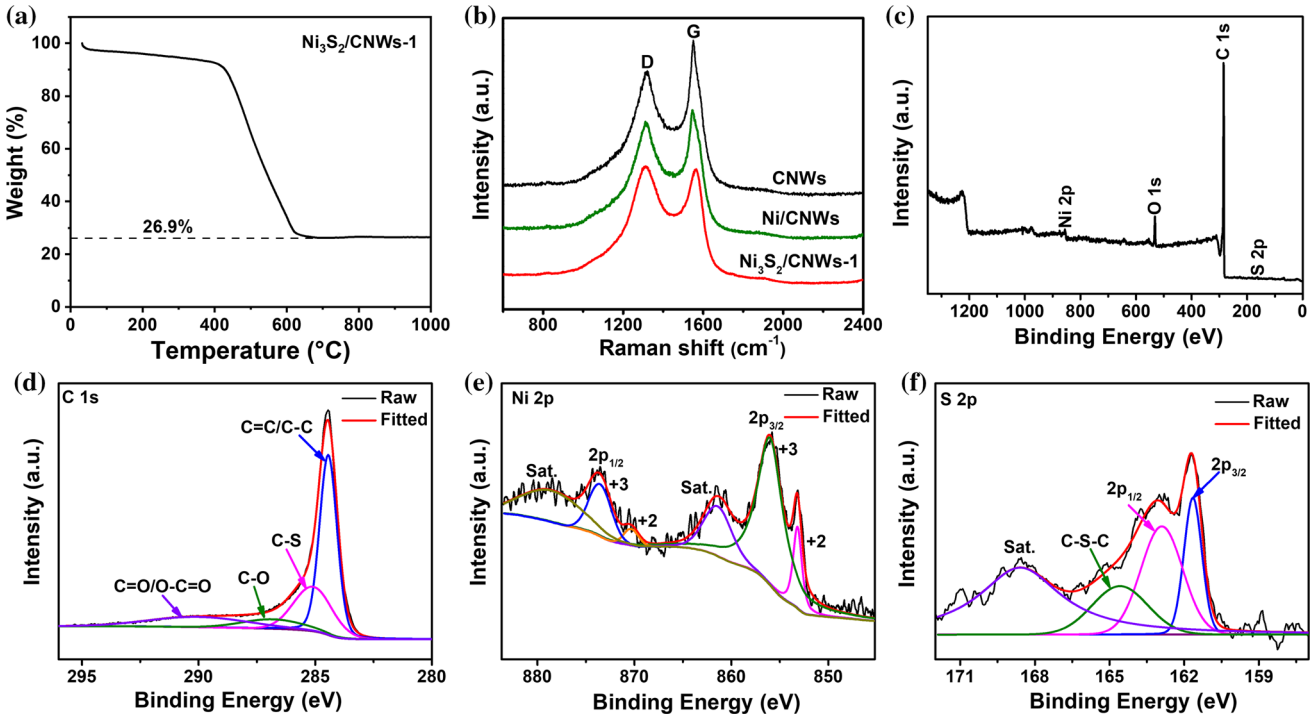

Figure 3 **a** TGA curve of Ni_3S_2/CNWs-1; **b** Raman spectra of CNWs, Ni/CNWs and Ni_3S_2/CNWs-1 samples; **c** XPS survey spectrum and **d**–**f** high-resolution XPS spectra of C 1s, Ni 2p, and S 2p of Ni_3S_2/CNWs-1.

calculation process is described in the Supporting Information.

The Raman spectrum of Ni_3S_2/CNWs-1 (Fig. 3b) shows two representative scattering vibrational modes at 1313 and 1566 cm^{-1}, which can be ascribed to the D band (defects) with disorder characteristics and the G band (sp^2 hybridization of carbon atoms) with graphite characteristics, respectively [19, 20]. I_D/I_G is the intensity ratio of the D band and G band, which reflects the surface defects of the active material and the distortion of the carbon lattice. Consequently, for the Ni_3S_2/CNWs-1 composite, the Ni/CNWs precursor and the control sample CNWs, the I_D/I_G values are determined to be 1.02, 0.92 and 0.82, respectively, indicating that the addition of sulfur source induces surface defects and produces sufficient Li-ion storage sites [16, 21].

The element composition and chemical valence state of the Ni_3S_2/CNWs-1 were evaluated by XPS analysis. Figure 3c shows the survey spectrum of the presence of nickel, sulfur, carbon and oxygen elements. Specifically, the nickel, sulfur and carbon elements are ascribed to the Ni_3S_2/CNWs composite, while the oxygen element is mainly attributed to the exposure of the sample to the air. The four major peaks of high-resolution C 1s spectrum (Fig. 3d) at 284.4, 285.1, 286.8, and 290.0 eV can be assigned to C–C/C=C, C–S, C–O, and C=O/O–C=O, respectively [22, 23]. The C–S covalent bond in the carbon nanowalls further confirmed that carbon host combines with some sulfur atoms to form a defective site, which is also consistent with the results of Raman spectroscopy analysis. Deconvolution of Ni 2p spectrum (Fig. 3e) produces two major strong peaks at 856.0 and 873.5 eV, which are ascribed to Ni $2p_{3/2}$ and Ni $2p_{1/2}$, respectively, demonstrating the trivalent valence of Ni in Ni_3S_2. And the intense peaks demonstrate that Ni^{3+} is the majority. Furthermore, the two peaks of Ni $2p_{3/2}$ and Ni $2p_{1/2}$ are located at 853.2 eV and 870.3 eV, respectively, indicating that the Ni element in Ni_3S_2 is a divalent state, and the weak peaks at 861.4 and 878.5 eV are satellite peaks [24, 25]. The two strong peaks of S 2p spectrum (Fig. 3f) at 161.7 and 162.9 eV are ascribed to S $2p_{3/2}$ and S $2p_{1/2}$, respectively, which are attributed to the metal-sulfur (M-S) bonds of Ni_3S_2. The peak with binding energy at 164.6 eV is associated with the C–S–C, revealing the perfect combination of sulfur atoms with conductive carbon nanowalls. Additionally, the peak at 168.6 eV corresponds to a satellite peak [26, 27]. The BET test was used to study the specific surface area and pore size distribution of

Ni_3S_2/CNWs-1. The N_2 adsorption–desorption isotherm of Ni_3S_2/CNWs-1 (Fig. S9a) exhibits a type IV with hysteresis loop, which is attributed to the presence of mesoporous characteristics in the composites [28, 29]. Note that the specific surface area of Ni_3S_2/CNWs-1 can be obtained from BET analysis is 484 m^2 g^{-1}. Meanwhile, the mesoporous structure can be further observed from the pore size distribution (Fig. S9b). In contrast, the specific surface areas calculated by the BET method for Ni_3S_2/CNWs-2, CNWs and Ni_3S_2 were 446, 490 and 86 m^2 g^{-1}, respectively. The abundant mesopores and suitable specific surface area are beneficial for the electrolyte immersion into the active material and enhance its electrochemical performance in the process of charging and discharging.

To clarify the electrochemical superiority of Ni_3S_2/CNWs-1 composite, we conducted the comparative study of Ni_3S_2/CNWs-2, CNWs and Ni_3S_2 in Fig. 4. We investigated the electrochemical behaviors of electrodes by performing Cyclic voltammetry (CV) tests within the potential range of 0.01–3.00 V. Figure 4a displays the initial three consecutive CV curves of the Ni_3S_2/CNWs-1 electrode at 0.1 mV s^{-1}. Two obvious peaks in the first cathodic scan at 1.31 and 1.61 V, which can be ascribed to the insertion of Li^+ into the electrode material and the reduction of Ni_3S_2 to Ni ($4Li^+ + 4e^- + Ni_3S_2 = 3Ni + 2Li_2S$). Also, it is worth noting that the peak at 0.66 V is generally attributed to the decomposition of organic electrolyte and the formation of solid electrolyte interface (SEI) layer. The main peak in the potential range of 0.02–0.15 V is related to lithium ions embedded in the carbon lattice, so this electrode material has lithium storage activity, which coincides with the trend of the CV curve of the CNWs electrode (Fig. S11a). It can be observed from the first anodic scan that the strong peak appearing at 1.96 V is due to the de-intercalation of Li^+ and the electrochemical decomposition of Li_2S followed by the oxidation of Ni to Ni_3S_2 ($3Ni + 2Li_2S = 4Li^+ + 4e^- + Ni_3S_2$) [30]. In the second cathodic scan, it can be directly observed that the peak of 0.66 V vanished, while the peak of 1.61 V moved to approximately 1.76 V, which was attributed to the irreversible phase transition of Ni_3S_2/CNWs-1 electrode material after the first lithium ion intercalation. After the second cycle, all redox peaks perfectly overlapped for the Ni_3S_2/CNWs-1 and CNWs electrodes, demonstrating the excellent stability of the SEI layer. Nevertheless, from the CV curves of Ni_3S_2/CNWs-2 (Fig. S10a) and Ni_3S_2 (Fig. S12a), it was observed that all redox peaks did not overlap, suggesting the inferior reversible performances.

The galvanostatic charge and discharge curves of the Ni_3S_2/CNWs-1 anode in the first three cycles when the current density is 200 mA g^{-1} are displayed in Fig. 4b. For the first cycle, the high discharge and charge capacities of Ni_3S_2/CNWs-1 were 1616 and 1056 mAh g^{-1}, respectively, and the corresponding coulombic efficiency was calculated to be 65.3%. From the charge and discharge curves, we can clearly observe a representative phenomenon, that is, the electrochemical reaction-driven electrolyte degradation to form a thin SEI film, which directly causes the loss of irreversible capacity. In the first discharge curve, a voltage plateau of 1.31 V is closely related to the reduction of Ni_3S_2 to Ni. For the first charge curve, a voltage plateau of 1.96 V is in connection with the oxidation of Ni to Ni_3S_2 during the conversion reaction. All charge–discharge voltage plateaus of the Ni_3S_2/CNWs-1, Ni_3S_2/CNWs-2 (Fig. S10b), CNWs (Fig. S11b) and Ni_3S_2 (Fig. S12b) anodes are consistent with the redox peaks of CV curves.

Figure 4c presents the cycle stability of the Ni_3S_2/CNWs-1 anode when the current density is 200 mA g^{-1}. Before the initial thirty cycles, the slow decay of capacity may be caused by the irreversible insertion of lithium into ultrafine pores. Interestingly, the discharge capacity of Ni_3S_2/CNWs-1 anode after cycling 200 times was 906 mAh g^{-1} and the coulombic efficiency reached 99.6%. By contrast, the discharge capacities of Ni_3S_2/CNWs-2, CNWs and Ni_3S_2 anodes after 200 cycles at 200 mA g^{-1} were 585, 570 and 355 mAh g^{-1}, respectively. These obvious differences can be explained by the following elaboration. The continuous and severe capacity decay of the Ni_3S_2/CNWs-2 and Ni_3S_2 electrodes during cycling may be ascribed to their inherent inferior conductivity and the inevitable aggregation and pulverization of Ni_3S_2 nanoparticles. The large electrode–electrolyte contact area of Ni_3S_2/CNWs-1 and CNWs anodes possess the 3D-interconnected porous structures, which can efficaciously inhibit the volume expansion of Ni_3S_2 in the electrochemical cycling, so these two electrodes exhibit better cyclic reversibility. For Ni_3S_2/CNWs-1 electrode, although Ni_3S_2 only possesses a theoretical capacity of 446 mAh g^{-1}, the combination effect of reversible capacity of CNWs

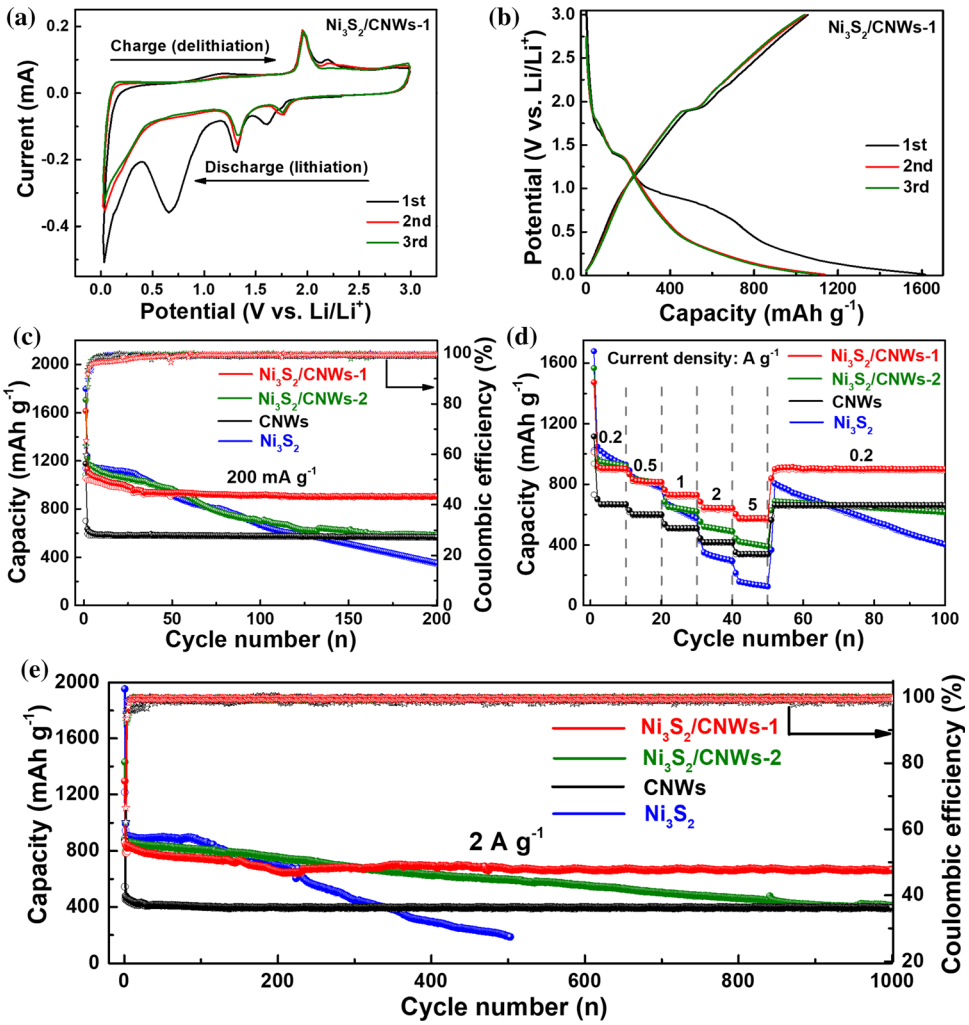

Figure 4 **a** CV curves and **b** charge–discharge curves of the Ni_3S_2/CNWs-1 anode at 1st, 2nd and 3rd cycle; **c** cycle performance at 200 mA g^{-1}; **d** rate performance, and **e** super-long cycling performance at 2 A g^{-1} for the Ni_3S_2/CNWs-1, Ni_3S_2/CNWs-2, CNWs and Ni_3S_2 anodes.

and Ni_3S_2 enhances the lithium storage performance of Ni_3S_2/CNWs-1 electrode.

The rate capability is also critical for evaluating the electrochemical properties of the anodes. Figure 4d displays the rate capability of Ni_3S_2/CNWs-1 anode when the current density changes from 0.2 to 5 A g^{-1}. The average reversible capacities of the Ni_3S_2/CNWs-1 were 905, 819, 729, 643, and 576 mAh g^{-1} when the current densities were 0.2, 0.5, 1, 2, and 5 A g^{-1}, respectively. It is worth noting that the reversible capacity of the Ni_3S_2/CNWs-1 anode is restored to 902 mAh g^{-1} when the current density is restored to 0.2 A g^{-1}, which is better than Ni_3S_2/CNWs-2 (616 mAh g^{-1}), CNWs (662 mAh g^{-1}) and Ni_3S_2 (405 mAh g^{-1}) anodes, further illustrating its outstanding reversibility. Figure S13a–d shows the corresponding charge–discharge profiles of the four anodes at various current densities.

The ultralong cycling performance of Ni_3S_2/CNWs-1 anode at 2 A g^{-1} is displayed in Fig. 4e. The initial discharge and charge capacities of Ni_3S_2/CNWs-1 anode are 1296 and 862 mAh g^{-1}, respectively. Also, the discharge capacity of Ni_3S_2/CNWs-1 (666 mAh g^{-1}) anode after 1000 cycles is higher than that of Ni_3S_2/CNWs-2 (407 mAh g^{-1}), CNWs (395 mAh g^{-1}) and Ni_3S_2 (192 mAh g^{-1}) anodes, and the capacity decay rate of each cycle is only 0.016%. Moreover, the coulombic efficiency of Ni_3S_2/CNWs-1 anode is as high as 99.6%, showing the excellent long-life cycle stability. Accordingly, the reversible capacity and cycle stability of the Ni_3S_2/CNWs-1 anode material are enhanced due to the synergistic combination of Ni_3S_2 nanoparticles with high theoretical capacity and carbon nanowalls with 3D porous structures. In addition, the well-designed mesoporous structure facilitates rapid transmission of Li^+ and electrons, so the Ni_3S_2/CNWs-1 anode

exhibits outstanding lithium storage properties. It can be observed that the enhanced lithium storage performance of Ni_3S_2/CNWs-1 composite is higher than that of other previously reported nickel sulfide anode materials (Table S1).

The superior electrochemical performance of Ni_3S_2/CNWs-1 anode is closely connected with its unique merits, as shown below: (1) the Ni_3S_2 nanoparticles are in situ encapsulated in the carbon nanowalls with 3D-interconnected porous structures, which can efficiently alleviate the larger volume expansion of Ni_3S_2 particles during cycling. (2) The abundant mesoporous structure is produced by the pyrolysis of pore-forming agent $KHCO_3$, which can provide a larger contact area and shorten the transmission route of electrons and Li^+ to enhance the kinetics. (3) The synergistic effect between uniformly dispersed Ni_3S_2 nanoparticles and conductive carbon nanowalls can greatly improve reversible capacity and cycle stability. As further evidence, the SEM and TEM images of Ni_3S_2/CNWs-1 (Fig. S14) and Ni_3S_2/CNWs-2 (Fig. S15) anodes were shown after 200 cycles at 200 mA g^{-1}. We can clearly observe that the overall morphology of the Ni_3S_2/CNWs-1 anode remains almost unchanged after cycling without obvious structural collapse, and the Ni_3S_2 nanoparticles and carbon nanowalls can also be distinctly identified, which proves the structural integrity of the Ni_3S_2/CNWs-1 composite.

Charge storage kinetics analysis based on CV tests was carried out at various scan rates to explore the lithium storage mechanism of Ni_3S_2/CNWs-1 (Fig. 5a–e). Figure 5a shows the CV curves of Ni_3S_2/CNWs-1 anode at the scanning rate of 0.1–1.0 mV s^{-1}. We can observe that the CV curve is almost free of distortion. Generally, the CV curves of different scanning rates are analyzed in combination with the following equations to calculate the contribution ratio of faradic and non-faradic (pseudocapacitive) to lithium storage [19, 31, 32]:

$$i = av^{b} \tag{1}$$

$$\log(i) = b\log(v) + \log(a) \tag{2}$$

$$i = k_1 v + k_2 v^{1/2} \tag{3}$$

where i is the peak current, v is the scanning rate, and a, b, k_1, and k_2 are tunable parameters. By analyzing Eqs. (1) and (2), it can be concluded that b = 1 and 0.5 correspond to the contribution of pseudo-capacitance and ion-diffusion, respectively [33, 34]. Figure 5b shows the b values of 1 (0.70) and 2 (0.81) peaks of Ni_3S_2/CNWs-1, indicating that the electrochemical reaction involves pseudo-capacitance contribution. Based on Eq. (3) and the analyzed k_1 and k_2 constants (Fig. 5c), we calculate the detailed pseudo-capacitance contribution at 0.7 mV s^{-1} (Fig. 5d). Specifically, when the scanning rates are 0.1, 0.3, 0.5, 0.7, and 1.0 mV s^{-1}, the pseudo-capacitance contributions of the Ni_3S_2/CNWs-1 anode (Fig. 5e) are 35.2%, 43.5%, 57.9%, 65.9%, and 76.6%, respectively, which manifests that the electrochemical charge–discharge process is dominated by the pseudocapacitive lithium storage, which also indicates that favorable capacitive kinetics of the Ni_3S_2/CNWs-1 anode contributes to outstanding lithium storage.

The electrochemical impedance spectroscopy (EIS) tests of Ni_3S_2/CNWs-1, Ni_3S_2/CNWs-2, CNWs and Ni_3S_2 anodes before (Fig. S16) and after 200 cycles (Fig. 5f) were performed to investigate the kinetic properties of electron/ion diffusion. In the Nyquist plots, the semicircle in the high-frequency region and the sloped straight line in the low-frequency region are associated with the charge-transfer resistance (R_{ct}) and the diffusion resistance of lithium ions (Warburg impedance) [35–37]. The Nyquist plots of the four anodes are fitted by the equivalent circuit (the inset of Fig. 5f). As displayed in Fig. S16, for the fresh half-cell, the charge-transfer resistance of the Ni_3S_2/CNWs-1 (58.0 Ω) anode is lower than that of Ni_3S_2/CNWs-2 (131.7 Ω), CNWs (64.4 Ω) and Ni_3S_2 (151.9 Ω), revealing its better conductivity. Additionally, after 200 cycles, the resistance of Ni_3S_2/CNWs-1 anode (Fig. 5f) at 200 mA g^{-1} was 55.0 Ω, which was smaller than that before the cycle, and also lower than that the Ni_3S_2/CNWs-2 (99.5 Ω), CNWs (115.4 Ω) and Ni_3S_2 (76.0 Ω) anodes after the cycle, further indicating its excellent conductivity. From the Nyquist plots, we can observe that the slope of the inclined line of Ni_3S_2/CNWs-1 anode is larger than that of the other three comparative anodes, suggesting its higher Li^+ diffusion coefficient, thus promoting the superior reaction kinetics and cycling performance in the electrochemical reaction.

The superior electrochemical performances of the aforementioned Ni_3S_2/CNWs-1 anode inspire us to study its practicability in full cell. According to the schematic illustration displayed in Fig. 6a, the button-type full cell is assembled by using Ni_3S_2/CNWs-1 anode and $LiFePO_4$ cathode. Figure S17 displays the electrochemical performance of $LiFePO_4$ cathode,

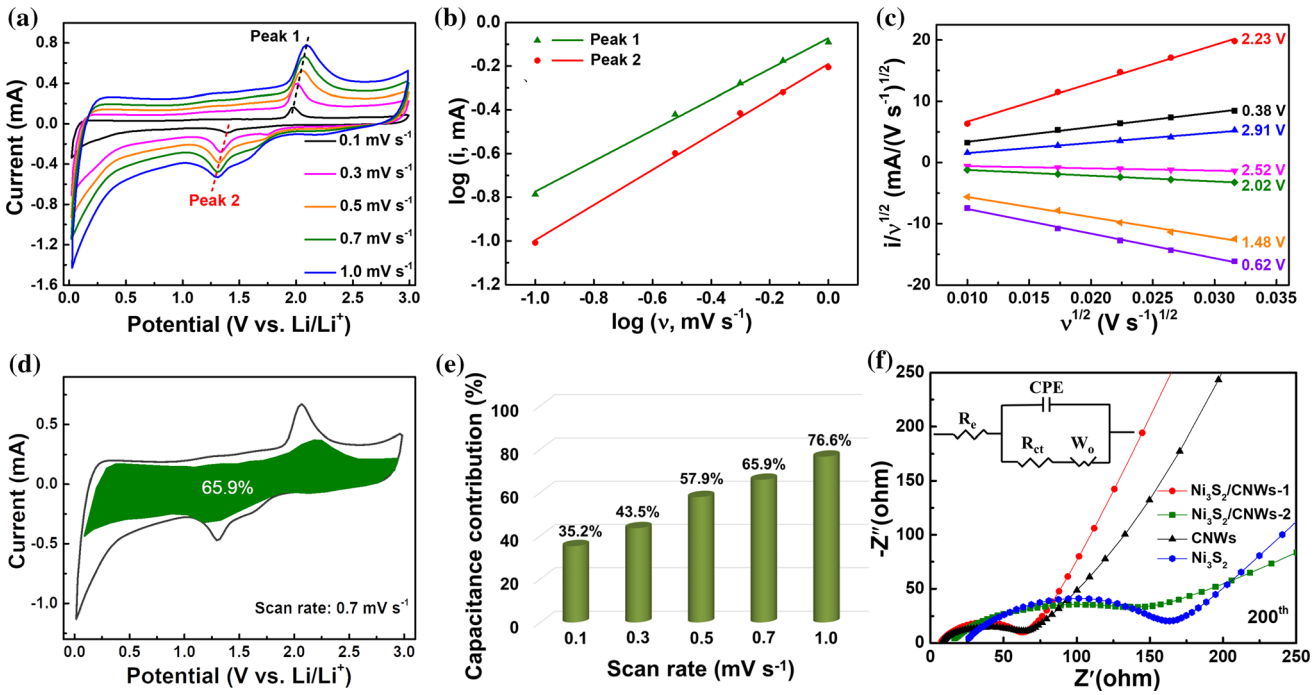

Figure 5 **a** CV curves of Ni_3S_2/CNWs-1 anode at various scanning rates; **b** relationship of log(i) versus log(v) of Ni_3S_2/CNWs-1 anode; **c** plots of $v^{1/2}$ versus $i/v^{1/2}$ at different redox states for obtaining k_1 and k_2 constants; **d** faradic (white) and non-faradic (green) contributions at 0.7 mV s^{-1}; **e** the pseudocapacitive contributions of the Ni_3S_2/CNWs-1 at various scanning rates; **f** Nyquist plots of the Ni_3S_2/CNWs-1, Ni_3S_2/CNWs-2, CNWs and Ni_3S_2 anodes after 200 cycles at 200 mA g^{-1} (inset: the equivalent circuit was fitted by EIS).

from which we can observe that the first charge capacity is 142 mAh g^{-1}. The charge–discharge curves of Ni_3S_2/CNWs-1‖$LiFePO_4$ full cell (Fig. 6b) at 100 mA g^{-1} under the potential window of 0.5–3.6 V. The button-type full cell delivers the charge and discharge capacities of 135 and 131 mAh g^{-1} in the first cycle, respectively. After cycling 200 times, the reversible capacity of full cell was 113 mAh g^{-1} and the corresponding capacity retention rate was 83.7% (Fig. 6c), indicating excellent cycle stability. It is attractive that the button-type Ni_3S_2/CNWs-1‖$LiFePO_4$ full cell (Fig. 6d) can power 33 light-emitting diodes, demonstrating its potential for practical applications.

Conclusions

In summary, an in situ encapsulation of Ni_3S_2 nanoparticles into carbon nanowalls with 3D porous structures have been fabricated successfully via a cation adsorption approach and a hydrothermal method. The Ni_3S_2/CNWs-1 anode shows good lithium storage capacity, ultra-stable cycle performance and superior rate performance for rechargeable LIBs. In addition, the assembled button-type Ni_3S_2/CNWs-1‖$LiFePO_4$ full cell delivers a reversible capacity of 113 mAh g^{-1} and a capacity retention rate of 83.7% after 200 cycles at 100 mA g^{-1}. Such excellent lithium storage properties are in connection with the unique advantages of the Ni_3S_2/CNWs-1 anode. Firstly, the carbon nanowalls with 3D-interconnected porous structures can provide the larger contact area and effectively inhibit the aggregation of Ni_3S_2 nanoparticles. Secondly, the Ni_3S_2 nanoparticles possess a high theoretical capacity due to its high lithium storage activity based on the conversion mechanism. Thirdly, the synergistic effect of Ni_3S_2 nanoparticles and conductive graphene sheets can greatly improve cycle stability. This work demonstrates that the as-prepared Ni_3S_2/CNWs-1 anode is a prospective high-performance LIB material.

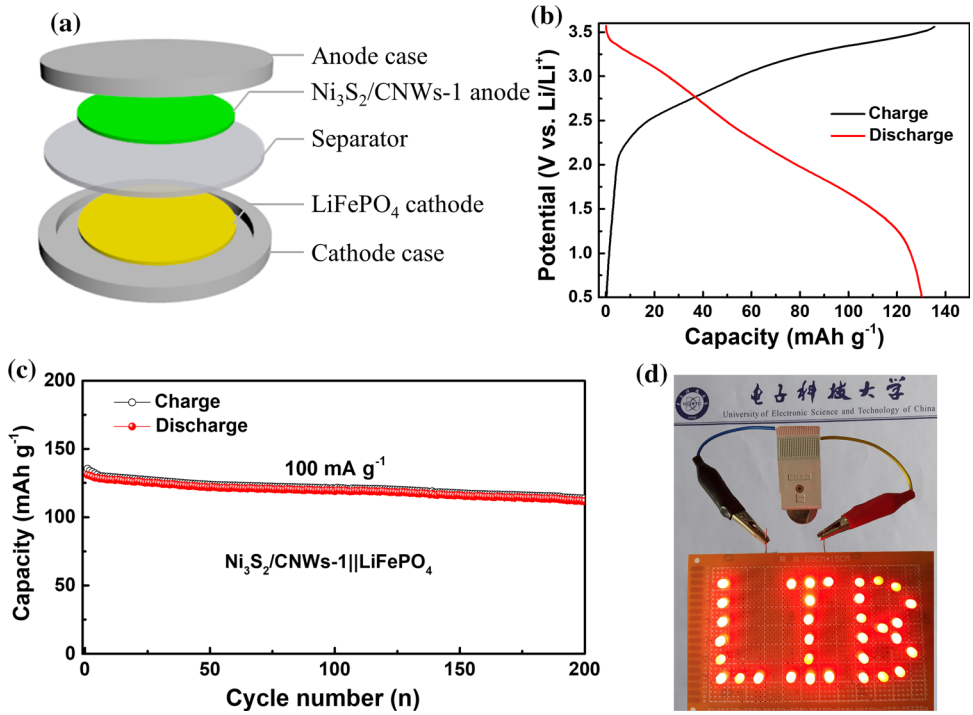

Figure 6 **a** Schematic diagram of the Li-ion full cell with Ni_3S_2/CNWs-1 as anode and $LiFePO_4$ as cathode; **b** charge–discharge curves of Ni_3S_2/CNWs-1||$LiFePO_4$ full cell at 0.1 A g^{-1}; **c** cycling performance of Ni_3S_2/CNWs-1||$LiFePO_4$ full cell; **d** The LEDs are illuminated by the as-assembled full cell.

Acknowledgements

This work was supported by the National Natural Science Foundation of China (Grant No. 51902040), the China Postdoctoral Science Foundation (No. 2017M622996), the China Postdoctoral Science Special Foundation (No. 2018T110959), the Sichuan Science and Technology Program (No. 19YYJC0129 and 20YYJC3821), and the Open Foundation of State Key Laboratory of Electronic Thin Films and Integrated Devices of UESTC (KFJJ201915).

Compliance with ethical standards

Competing interest The authors declared that there is no conflict of interest.

Electronic supplementary material: The online version of this article (https://doi.org/10.1007/s10853-020-05203-3) contains supplementary material, which is available to authorized users.

References

[1] Wu N, Yang Y, Jia T, Li T, Li F, Wang Z (2020) Sodium-tin metal-organic framework anode material with advanced lithium storage properties for lithium-ion batteries. J Mater Sci 55:6030–6036. https://doi.org/10.1007%2Fs10853-020-04436-6

[2] Shuang W, Kong L, Zhong M, Wang D, Liu J, Bu XH (2018) Rational design of Co embedded N, S-codoped carbon nanoplates as anode materials for high performance lithium-ion batteries. Dalton Trans 47:12385–12392

[3] Yu XW, Manthiram A (2018) Electrode-electrolyte interfaces in lithium-based batteries. Energy Environ Sci 11:527–543

[4] Meng L, Guo R, Li F, Ma Y, Peng J, Zhao J, Sang Z, Li T, Luo Y, Lu Y, Sun X (2020) Hierarchical porous $Li_xV_2O_4$/C anode assembled with nanoflake for high-performance lithium-ion battery. J Mater Sci 55:5522–5533. https://doi.org/10.1007/s10853-020-04388-x

[5] Liu Y, Zhong M, Kong L, Li A, Sun X, Wang D, Bu XH (2019) $Fe_{1-x}S$/nitrogen and sulfur co-doped carbon composite derived from a nanosized metal-organic framework for high-performance lithium-ion batteries. Inorg Chem Front 6:50–56

[6] Duan W, Yan W, Yan X, Munakata H, Jin Y, Kanamura K (2015) Synthesis of nanostructured Ni_3S_2 with different morphologies as negative electrode materials for lithium ion batteries. J Power Sources 293:706–711

[7] Geng H, Kong SF, Wang Y (2014) NiS nanorod-assembled nanoflowers grown on graphene: morphology evolution and Li-ion storage applications. J Mater Chem A 2:15152–15158

[8] Lin YM, Qiu ZZ, Li DZ, Ullah S, Hai Y, Xin HL, Liao WD, Yang B, Fan HS, Xu J, Zhu CZ (2018) NiS_2@CoS_2 nanocrystals encapsulated in N-doped carbon nanocubes for

high performance lithium/sodium ion batteries. Energy Storage Mater 11:67–74

[9] Jin RC, Zhou JH, Guan YS, Liu H, Chen G (2014) Mesocrystal Co_9S_8 hollow sphere anodes for high performance lithium ion batteries. J Mater Chem A 2:13241–13244

[10] Wang Y, Niu YB, Li CM (2017) The effect of the morphologies of Ni_3S_2 anodes on the performance of lithium-ion batteries. ChemSel 2:4445–4451

[11] Zhang S, Lin R, Yue W, Niu F, Ma J, Yang X (2017) Novel synthesis of metal sulfides-loaded porous carbon as anode materials for lithium-ion batteries. Chem Eng J 314:19–26

[12] Li D, Li X, Hou X, Sun X, Liu B, He D (2014) Building a Ni_3S_2 nanotube array and investigating its application as an electrode for lithium ion batteries. Chem Commun 50:9361–9364

[13] Du JM, Kang DJ (2007) A shape-controlled method to functionalize multiwalled carbon nanotubes with Ni_3S_2. Inorg Chem 46:10307–10311

[14] Wu XY, Li SM, Xu YY, Wang B, Liu JH, Yu M (2019) Hierarchical heterostructures of NiO nanosheet arrays grown on pine twig-like beta-NiS@Ni_3S_2 frameworks as free-standing integrated anode for high-performance lithium-ion batteries. Chem Eng J 356:245–254

[15] Jiang JL, Ma C, Yang YB, Ding JJ, Ji HM, Shi SJ, Yang G (2018) Synergetic interface between NiO/Ni_3S_2 nanosheets and carbon nanofiber as binder-free anode for highly reversible lithium storage. Appl Surf Sci 441:232–238

[16] Guerra A, Achour A, Vizireanu S, Dinescu G, Messaci S, Hadjersi T, Boukherroub R, Coffinier Y, Pireaux JJ (2019) ZnO/carbon nanowalls shell/core nanostructures as electrodes for supercapacitors. Appl Surf Sci 481:926–932

[17] Kim AY, Ardhi REA, Liu G, Kim JY, Shin HJ, Byun D, Lee JK (2019) Hierarchical hollow dual Core-Shell carbon nanowall-encapsulated p–n SnO/SnO_2 heterostructured anode for high-performance lithium-ion-based energy storage. Carbon 153:62–72

[18] Wang XH, Shi B, Wang XQ, Gao J, Zhang C, Yang ZZ, Xie HF (2017) One-step synthesis of V_2O_5/Ni_3S_2 nanoflakes for high electrochemical performance. J Mater Chem A 5:23543–23549

[19] Liu W, Xu H, Qin H, Lv Y, Zhu G, Lei X, Lin F, Zhang Z, Wang L (2020) Rapid coating of asphalt to prepare carbon-encapsulated composites of nano-silicon and graphite for lithium battery anodes. J Mater Sci 55:4382–4394. https://doi.org/10.1007/s10853-019-04313-x

[20] Huang P, Zhang M, Kang J, Feng H, Su Q, Du G, Yu Y, Xu B (2019) Rapid microwave-irradiation synthesis of $ZnCo_2O_4$/ZnO nanocrystals/carbon nanotubes composite as anodes for high-performance lithium-ion battery. J Mater Sci 54:4154–4167. https://doi.org/10.1007/s10853-018-3119-1

[21] Shuang W, Huang H, Kong LJ, Zhong M, Li A, Wang DH, Xu YH, Bu XH (2019) Nitrogen-doped carbon shell-confined Ni_3S_2 composite nanosheets derived from Ni-MOF for high performance sodium-ion battery anodes. Nano Energy 62:154–163

[22] Wang W, Zeng P, Li J, Zhao Y, Chen M, Shao J, Fang Z (2018) Ultrathin nanosheets assembled hierarchical Co/NiS_x@C hollow spheres for reversible lithium storage. ACS Appl Nano Mater 1:3435–3445

[23] Kong L, Zhu J, Shuang W, Bu XH (2018) Nitrogen-doped wrinkled carbon foils derived from MOF nanosheets for superior sodium storage. Adv Energy Mater 8:1801515

[24] Li J, Li J, Chen T, Lu T, Mai W, Pan L (2019) Metal chelate induced in situ wrapping of Ni_3S_2 nanoparticles into N, S-codoped carbon networks for highly efficient sodium storage. Inorg Chem Front 6:694–704

[25] Tang T, Cui S, Chen W, Hou H, Mi L (2019) Bio-inspired nano-engineering of an ultrahigh loading 3D hierarchical Ni@$NiCo_2S_4$/Ni_3S_2 electrode for high energy density supercapacitors. Nanoscale 11:1728–1736

[26] Qie L, Chen WM, Xiong XQ, Hu CC, Zou F, Hu P, Huang YH (2015) Sulfur-doped carbon with enlarged interlayer distance as a high-performance anode material for sodium-ion batteries. Adv Sci 2:1500195

[27] Wang F, Zhu Y, Tian W, Lv X, Zhang H, Hu Z, Zhang Y, Ji J, Jiang W (2018) Co-doped Ni_3S_2@CNT arrays anchored on graphite foam with a hierarchical conductive network for high-performance supercapacitors and hydrogen evolution electrodes. J Mater Chem A 6:10490–10496

[28] Xu H, Zhu G, Hao B (2020) Metal-organic frameworks derived flower-like Co_3O_4/nitrogen doped graphite carbon hybrid for high-performance sodium-ion batteries. J Mater Sci Technol 35:100–108

[29] Wang C, Han Q, Xie R, Wang B, He T, Xie W, Tang Q, Li Y, Xu J, Yu B (2020) Fabrication of petal-like Ni_3S_2 nanosheets on 3D carbon nanotube foams as high-performance anode materials for Li-ion batteries. Electrochim Acta 331:135383

[30] Zhu JS, Hu GZ (2016) Facile synthesis of three-dimensional porous Ni_3S_2 electrode with superior lithium ion storage. Mater Lett 166:307–310

[31] Zhao C, Shen Z, Tu F, Hu Z (2020) Template directed hydrothermal synthesis of flowerlike $NiSe_x$/C composites as lithium/sodium ion battery anodes. J Mater Sci 55:3495–3506. https://doi.org/10.1007/s10853-019-04200-5

[32] Ge P, Zhang C, Hou H, Wu B, Zhou L, Li S, Wu T, Hu J, Mai L, Ji X (2018) Anions induced evolution of Co_3X_4 (X = O, S, Se) as sodium-ion anodes: The influences of electronic

structure, morphology, electrochemical property. Nano Energy 48:617–629

[33] Song Y, Chen ZL, Li YM, Wang QC, Fang F, Zhou YN, Hu LF, Sun DL (2017) Pseudocapacitance-tuned high-rate and long-term cyclability of $NiCo_2S_4$ hexagonal nanosheets prepared by vapor transformation for lithium storage. J Mater Chem A 5:9022–9031

[34] Hou BH, Wang YY, Liu DS, Gu ZY, Feng X, Fan HS, Zhang TF, Lü CL, Wu XL (2018) N-doped carbon-coated $Ni_{1.8}$-$Co_{1.2}$Se4 nanoaggregates encapsulated in N-doped carbon nanoboxes as advanced anode with outstanding high-rate and low-temperature performance for sodium-ion half/full batteries. Adv Funct Mater 28:1805444

[35] Zhang Z, Zhao H, Xia Q, Allen J, Zeng Z, Gao C, Li Z, Du X, Świerczek K (2016) High performance Ni_3S_2/Ni film with three dimensional porous architecture as binder-free anode for lithium ion batteries. Electrochim Acta 211:761–767

[36] Dong X, Deng ZP, Huo LH, Zhang XF, Gao S (2019) Large-scale synthesis of NiS@N and S co-doped carbon mesoporous tubule as high performance anode for lithium-ion battery. J Alloys Compd 788:984–992

[37] Fan HS, Yu H, Wu XL, Zhang Y, Luo ZZ, Wang HW, Guo YY, Madhavi S, Yan QY (2016) Controllable preparation of square nickel chalcogenide (NiS and $NiSe_2$) nanoplates for superior Li/Na ion storage properties. ACS Appl Mater Inter 8:25261–25267